

Article

Numerical Study of Aerodynamic Coefficients of a Ground Vehicle

Ferrari, J.M.S.¹, Kayser, F.M.², Noieto, L.G.³ and Goulart, J.N.V.⁴

¹ GMEC, Universidade de Brasília; jalusaferrari@gmail.com

² GMEC, Universidade de Brasília; fabio_mk_66@hotmail.com

³ Universidade de Brasília; lucianonoieto@gmail.com

⁴ GMEC, Universidade de Brasília; jvazgoulart@gmail.com

Received: 06/11/2020; Accepted: 05/12/2020; Published: 31/12/2020

Abstract: The objective of the present paper is to evaluate the turbulent flow around the Ahmed body immersed in air and to determine its aerodynamic coefficients for different slant angles. The bidimensional non-stationary analysis of an incompressible flow around the Ahmed body is carried out for three different rear angles which are 0°, 10° and 25°. The numerical simulations were performed under the same Reynolds number, $Re_L = 94\ 000$, based on the free streamwise velocity, u_∞ , the longitudinal length of the Ahmed body, L , and the kinematic viscosity of the work fluid, ν . The additional diffusivity caused by the turbulent motion was approached using the Boussinesq's idea through the k- ω SST. In the paper, aerodynamic coefficients of drag and the pressure and velocity fields are presented to characterize the Ahmed body for such slant angles, as well as the flow detachment point, determined through the dimensionless skin friction factor distribution on the body's surface. The results showed that the slant presence affects the skin friction and pressure coefficients. As the slant angle was increased, the portion of pressure drag became more significant in total drag. Skin friction coefficient distribution was first presented for this body. As numerical simulations were compared with available results in open literature and showed agreement, we concluded that it was possible to simulate a problem notably tridimensional with a bidimensional simulation, leading to savings in simulation time and computational cost.

Keywords: Ahmed body. CFD. k- ω SST. Q-criterion. skin friction factor.

1. Introduction

Aerodynamics is the study of resulting forces from the movement of a fluid through a body and is an important part of the vehicle design process. The fuel consumption of a vehicle associated with its movement is directly related to aerodynamic characteristics, such as the aerodynamic drag of the vehicle which is expressed as the drag coefficient, C_d (Ortega and Salari, 2005).

The understanding of vehicular aerodynamics is accomplished by also understanding the effect of the forces acting on the vehicle and how they arise. Consequently, detailed knowledge about flow characteristics and their relationship with body geometry is necessary for the design of new vehicles (Tunay et al., 2014). According to Wang et al. (2017), 10% reduction in drag forces could reduce the fuel consumption by 7%. Ground vehicles are considered as blunt bodies near a flat surface that represents the ground. Complex structures, such as cavities and wheels under rotation, make the flow completely three-dimensional (Hucho, 2013). The drag vehicle is strongly depending on how the flow behaves along the vehicle.

The number of structures that are immersed in the fluid and, therefore, subjected to the forces acting on their surfaces is infinite. Each one is characterized by shape, size, sharp or round angles, which yields new forces distribution and, therefore, different drag and lift coefficients. For this reason, many bodies are studied using an approach that relates the flow characteristics with the one found around a flat plate, a sphere or a cylinder (Daugherty, 1989). The approach using a similar geometry is often used for a simplified study or as an initial design

idea. The Ahmed body is a geometric simplification of an automobile vehicle and was chosen as the object of this study.

The Ahmed body was first presented in the study by Ahmed et al. (1984) with an experimental analysis of 3D flow in the body. The author's main objective was to verify the behavior of the drag coefficient, C_d , and the characteristics of the flow according to the variation of the rear angle. Ahmed body combines the essential geometric characteristics that determine the shape, length and flow separation zone. For the numerical simulation, to describe the flow around Ahmed body is still a challenge. This occurs, mainly, due to the correct prediction of drag and lift coefficients consistent with the experiment carried out by Ahmed et al. (1984) and other authors on the subject.

According to Li et al. (2017), there has been an urgency to develop new control devices for fuel consumption and greenhouse gas emission without compromising the vehicle aesthetics. Essel et al. (2020) affirms that understanding the wake characteristics between two in-line vehicles is also relevant to improve this question. Siddiqui and Chaab (2020) studied a simple passive device to drag reduction in Ahmed body using the $k-\omega$ SST model, one of the two methods suggested by Choi et al. (2014), active and passive, to reduce pressure drag. But Chovet et al. (2020) also affirms that a large portion the controllers are derived using the previous knowledge of the physics of the flow.

In this regard, this work aims to evaluate the drag coefficient of Ahmed's body with different slant angles under a turbulent flow with Reynolds of 94 000, based on the body's length, L , and the free stream velocity, u_∞ . It is also a purpose to identify the pressure distribution at the surface and the flow detachment point.

The main challenge that the work proposes is to simulate a problem notably tridimensional through bidimensional approach using Ansys CFX. The turbulence model used is $k-\omega$ SST, due to its ability to predict the boundary layer detachment and reattachment phenomena when compared to $k-\epsilon$ and $k-\omega$ models (Menter et al., 2003). In addition, Korkischko and Meneghini (2006) and Rafee and Moghimi (2018) found that the $k-\omega$ SST presents a good agreement with their experimental work with Ahmed body. The dimensions used in the computational domain are based in Korkischko and Meneghini (2006), but the Reynolds number used in the present work was lower. Furthermore, the work is also aimed to assess the relationship between the aerodynamics coefficients and slant angles, as well as the flow separation point.

2. Geometry and Numerical Procedure

2.1 Ahmed body

The dimensions of Ahmed body used in simulations of the present work are similar to that proposed by Ahmed et al. (1984) and are shown in Figure 1.

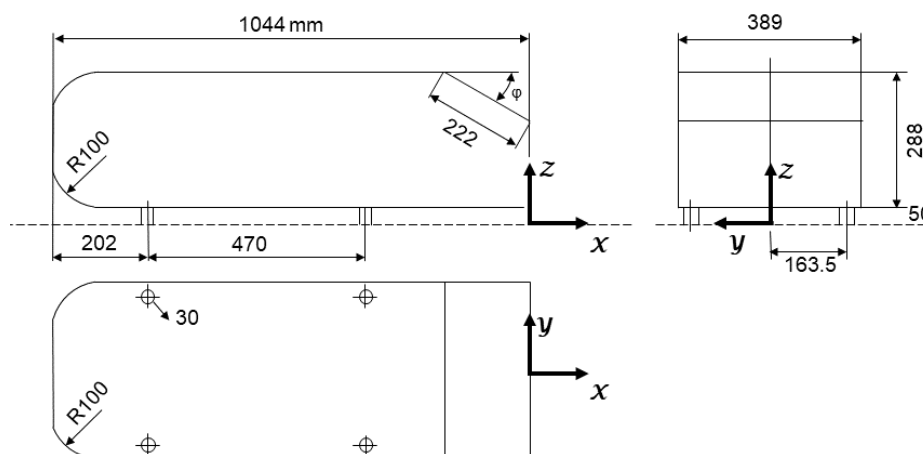


Figure 1. Dihedral view with body dimensions in mm (Ahmed et al., 1984).

Figure 2 shows the computational domain with dimensions in terms of the longitudinal length, L , of the body. The body is 50 mm above ground in all simulations, assigned by the letter "h". The body domain is placed at $3.5L$, downstream the entrance and its rear part is $8L$ away from the domain's outlet. The upper free surface of the computational domain is far enough from the body, being $5L$. The free stream velocity $u_\infty = 1.29$ m/s is imposed at inlet (A). Velocity components in the other directions are zero ($v = w = 0$). The turbulent intensity at (A) is 1% applied at the

free stream velocity. On body surfaces (B) non-slip conditions and impermeability are applied. At the outlet (C) a null differential pressure condition is applied.

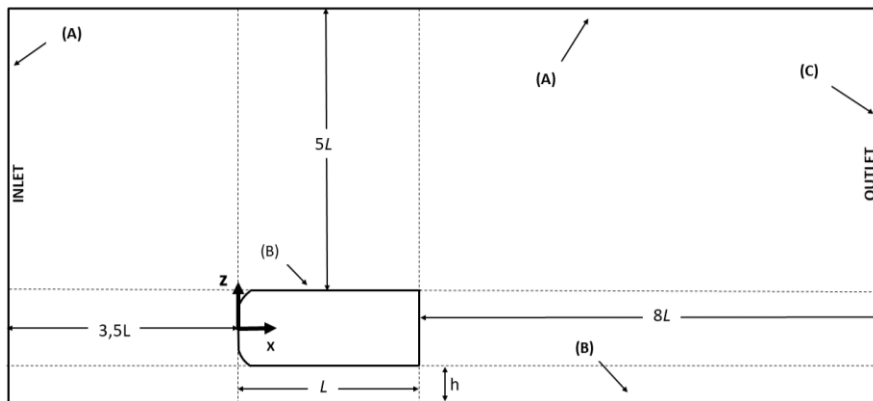


Figure 2. Description of the dimensions computational domain based at Korkischko and Meneghini (2006).

The rear slat angles used are $\varphi = 0^\circ, 10^\circ$ and 25° . The slant dimension was kept at 222 mm , as seen in Figure 3a. Those angles were chosen to assess the relationship between the rear angle and the aerodynamic coefficients. Figure 3b shows the reference points at the upper surface (1-2).

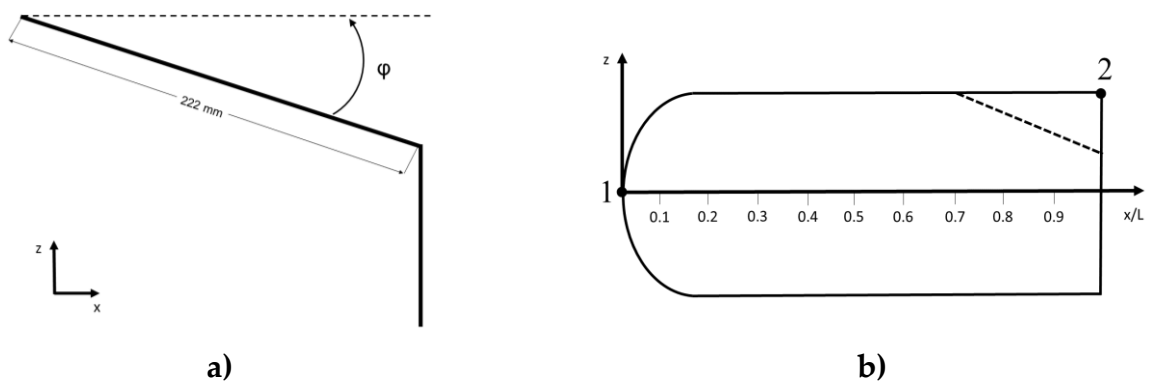


Figure 3. Schematic of Ahmed body: a) Slant angle and b) Surface reference points.

A mesh analysis was performed in the stationary phase for the two-dimensional domain with $\varphi = 25^\circ$ and the results are displayed in Table 1. The mesh was constructed with hexahedral volumes and this process resulted in a mesh with 54 998 nodes and 26 960 elements. The number of layers close to the wall was sufficient to obtain a $y^+ = 1$ with a growth rate of 1.2 in relation to the node closest to the wall.

Table 1. Mesh analysis for C_d with $\varphi = 25^\circ$ and $Re = 94\ 000$.

C_d	Nodes	Elements
0,51	50 868	24 899
0,48	55 396	27 114
0,49	68 658	33 623
0,47	54 998	26 960
0,47	58 430	28 620

The body with $\varphi = 25^\circ$ was used as a benchmark, since Bello-Millán et al. (2016) proposed an algebraic equation for drag evaluation over a vast Reynolds number range for this body. The algebraic equation was tested facing their experimental values and other external authors. The resultant mesh was able to achieve a good agreement with their work presenting an error around 8%. According to Bello-Millán et al. (2016), this equation is enough to provide C_d value for a Ahmed body for a Reynolds number ranging from 10^5 up to 6.96×10^6 :

$$C_d = 0.3849 + 0.0603e^{\frac{A}{0.5217}} \quad (1)$$

$$A = \frac{Re_t}{10^6}$$

In the time-dependent simulation, the time step was $\Delta t = 1.1 \times 10^{-4}$ s and this was kept for the three simulated cases. Time discretization was carried out by using the backward Euler scheme for time discretization. The advective terms of Navier-Stokes equations were solved by using Upwind Second Order scheme and the convergence criterion was set 10^{-5} , at least, for any equation.

To initialize the time-dependent runs, stationary field was prescribed as a first time step response. Courant number was kept less than one. The averaging process for each quantity was carried out over for about 19 s, leading to 3 flow-through times.

2.2 Governing Equations

According to Deschamps (2002), for incompressible flow, Equations 2 and 3 rule the mass conservation and the momentum, respectively:

$$\frac{\partial \bar{u}_i}{\partial x_i} = 0 \quad (2)$$

$$\frac{\partial \bar{u}_i}{\partial t} + \bar{u}_j \frac{\partial \bar{u}_i}{\partial x_j} = -\frac{1}{\rho} \frac{\partial \bar{P}}{\partial x_i} + \frac{\partial}{\partial x_j} \left[(v + v_t) \left(\frac{\partial \bar{u}_i}{\partial x_j} + \frac{\partial \bar{u}_j}{\partial x_i} \right) \right] \quad (3)$$

Where \bar{u}_i represents the velocity vector components, x_i is the spatial coordinates, \bar{P} is the thermodynamic pressure, ρ is the fluid density, v and v_t are the molecular and turbulent kinematic viscosity, respectively. Deschamps (2002) affirms that the additional momentum diffusivity, which is caused by the closure problem of the turbulence, is represented by the turbulent viscosity, v_t , that is approximate through the Boussinesq's idea described as:

$$\tau_{ij} = v_t \left(\frac{\partial \bar{u}_i}{\partial x_j} + \frac{\partial \bar{u}_j}{\partial x_i} \right) - \frac{2}{3} \delta_{ij} k \quad (4)$$

τ_{ij} is the Reynolds tensor, which is obtained through the decomposition of the non-linear terms of Navier-Stokes equation, and k represents the turbulent kinetic energy. So, additional equations are needed to raise up the turbulent kinematic viscosity, which is computed as a function of the turbulent kinetic energy field, k , and the specific rate of dissipation, ω . The k - ω SST model is a two equations turbulence model first introduced by Menter (1994). The model combines the advantages from k - ϵ model and k - ω model by a blending function that switches whenever it is possible. The k - ω SST model contains a cross-diffusion damping term from equation ω and results from k - ϵ model coupled to k - ω model by blending functions. As pointed by Severino et al. (2018), the k - ϵ model is used far from the wall region and near the wall is applied the k - ω model. According to Menter (1994), this two-equation model is ruled by the set of Equation 5-8.

$$\frac{\partial k}{\partial t} + \bar{u}_j \frac{\partial k}{\partial x_j} = \frac{\tau_{ij}}{\rho} \frac{\partial \bar{u}_i}{\partial x_j} - \beta^* \omega k + \frac{\partial}{\partial x_j} \left[(v + \sigma_k v_t) \frac{\partial k}{\partial x_j} \right] \quad (5)$$

$$\frac{\partial \omega}{\partial t} + \bar{u}_j \frac{\partial \omega}{\partial x_j} = \frac{\gamma \tau_{ij}}{v_t \rho} \frac{\partial \bar{u}_i}{\partial x_j} - \beta \omega^2 + \frac{\partial}{\partial x_j} \left[(v + \sigma_\omega v_t) \frac{\partial \omega}{\partial x_j} \right] + 2(1 - F_1) \frac{\sigma_{\omega 2}}{\omega} \frac{\partial k}{\partial x_j} \frac{\partial \omega}{\partial x_j}$$

The blending function is F_1 , which computes how far from the walls the problem is being solved and is defined as:

$$F_1 = \tanh(\arg^4)$$

$$\arg = \min \left[\max \left(\frac{\sqrt{k}}{\beta^* \omega d}, \frac{500v}{d^2 \omega} \right), \frac{4\rho \sigma_{\omega 2} k}{CD_{k\omega} d^2} \right] \quad (6)$$

Within the boundary layer region, F_1 is one and the k- ω model is activated. Outside the boundary layer, F_1 is zero and k- ϵ model must be activated. Finally, the turbulent kinematic viscosity is calculated through:

$$v_t = \frac{a_1 k}{\max(a_1 \omega, \square F_2)} \quad (7)$$

Where \square is the absolute value of the vorticity and a_1 is a closure coefficient that is set to 0.30. F_2 is the second blending function defined as:

$$F_2 = \tanh \left[\max \left(\frac{2\sqrt{k}}{\beta^* \omega y}, \frac{500\nu}{y^2 \omega} \right) \right]^2 \quad (8)$$

3. Results

3.1. Pressure and Drag Coefficients

In the next figures, the pressure and skin friction coefficients distribution on the body's surface are stressed. Both are shown in dimensionless form as follow:

$$C_p = \frac{\rho - \rho_0}{\frac{1}{2} \rho u_\infty^2} \quad (9)$$

$$C_f = \frac{\tau_w}{\rho u_\infty^2} \sqrt{\text{Re}_l}$$

C_p and C_f are the pressure and skin friction coefficients, respectively, ρ and τ_w are the pressure and the stress on the walls as a function of the position. Whereas ρ_0 is the reference pressure, ρ is the fluid density and u_∞ is the free stream velocity in x-direction. The points shown in Figure 2b marks reference points on the surface of Ahmed body. The following results are presented along the body between points 1 and 2.

The flow separation is characterized by an adverse pressure gradient, where fluid particles lose kinetic energy due to friction. This situation leads to a zero velocity at the surface and, consequently, a zero-stress location is highlighted, being straightforward to identify the flow detachment.

So, the flow separation takes place wherever τ_w is null on the contour of the body. The shear stress is null whenever:

$$\left. \frac{\partial \bar{u}}{\partial n} \right| = 0 \text{ in } \Gamma \quad (10)$$

Figure 4 (a-c) shows the pressure coefficient at the upper side of the bodies for slant angles of 0° , 10° and 25° , respectively. It was observed that the presence of a slant changes the pressure coefficient distribution. For the three cases, the maximum pressure was seen to take place at the frontal region, at the body's stagnation point, decreasing downstream.

For body with slant angle $\varphi = 0^\circ$ the pressure coefficient assumes the minimal value at about $x/L = 0.10$, yielding $C_p = -2.4$. The same minimum value was observed for the two other cases, at $x/L = 0.38$ for the case with $\varphi = 10^\circ$ and at $x/L = 0.4$ for $\varphi = 25^\circ$. The simulations showed a remarkable difference with the presence of a rear slant angles, but it was not significant when the angle increased. It was interesting to note that highest pressure point for the rear slant body of 25° takes place at further position in comparison to the other geometries, meaning that the stagnation point has displaced towards the upper surface of the body.

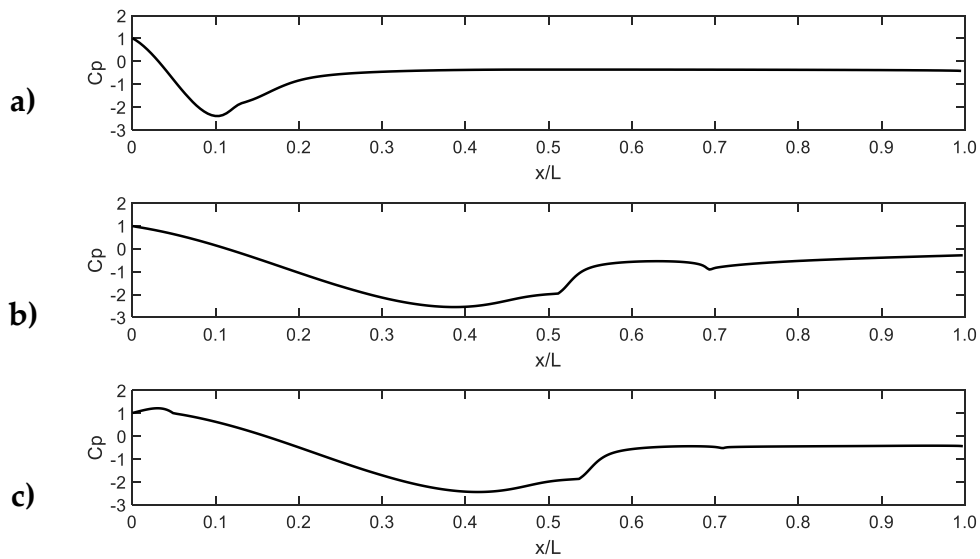


Figure 4. Pressure coefficients for slant angles: a) 0°, b) 10° and c) 25°.

In the three cases, most part of the body are under negative values of pressure. Negative pressure values were well reported by Bruneau et al. (2014), who also stated that such low-pressure region behind the Ahmed body was resulted from the generated vortices at rear region. Although the behavior of the C_p is different along the body, the same value was found at the end of them for any rear slant angle.

At around $x/L = 0.7$, the slant region begins for cases with $\varphi = 10^\circ$ and 25° . It is possible to identify a local minimum, so that one can speculate to have a separation bubble or a flow jump happening in that region, as mentioned by Shadmani et al. (2018). Shadmani et al. (2018) also observed the C_p growth at slanted surface.

As said before the flow detachment can be identified through the skin friction coefficient, whenever $C_f = 0$. Figure 5 (a – c) shows the skin friction coefficient at the upper side of the bodies for the simulated slant angles of 0° , 10° and 25° . We can see the rear slat angle play important role on this regard. In the first case, $\varphi = 0^\circ$, the flow is seen detached in the front region at about $x/L = 0.12$ and reattached at 0.19 (Figure 5a). The skin friction coefficient decreases again near the body rear where should be expected a flow complete detachment behind the body.

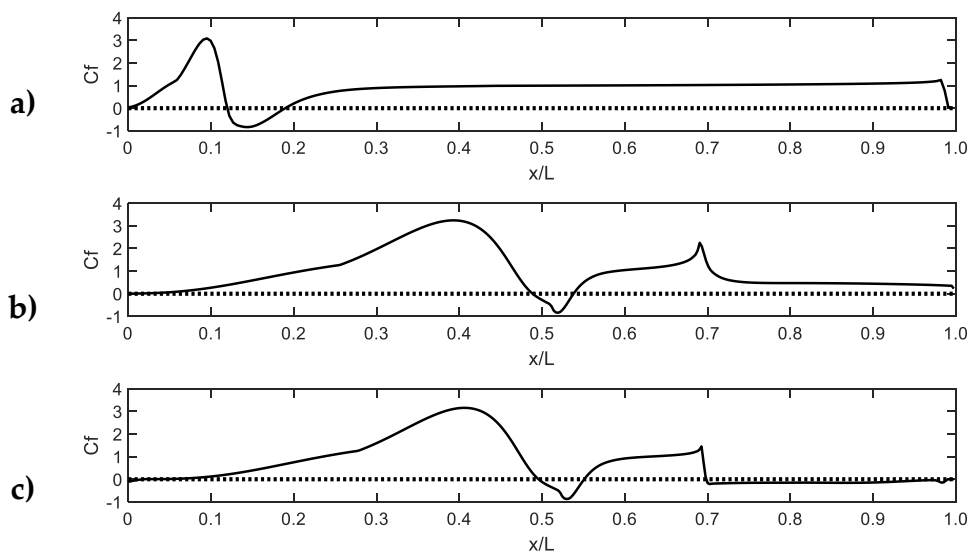


Figure 5. Skin friction coefficients for slant angles: a) 0°, b) 10° and c) 25°.

With regard to the other two geometries, where the slant angle was increased, the skin friction coefficient distribution is completely different from the first case. In both pictures Figure 5 (b and c), the null skin friction is seen

at $x/L = 0.49$. The flow seems to reattaches again short after, indicating a separation bubble on the upper side of the body in both cases are the same. In Figure 5c, the reader can see the null skin friction again at $x/L = 0.7$, right where the slanted region begins. It is interesting to note that the slat increasing from 10° to 25° stress different C_f distribution nearby the rear part of the body. The $\varphi = 10^\circ$ body simulation did not show null C_f point after the reattaching flow.

3.2. Q Criterion

To identify coherent structures around the body, it was used the Q criterion, first proposed by Hunt et al. (1988). Such methodology has been used successfully afterwards (Goulart et al., 2016, Candela et al., 2020). Furthermore, through this visualization help us to raise awareness how such instabilities can impact in the process of momentum and heat diffusion, for instance (Ferrari et. al, 2016).

The idea behind the analyses is to discover the flow regions where the vorticity overpasses the shear strain rate. The Q parameter is defined here as:

$$Q = \frac{1}{2} (|\Omega|^2 - |S|^2) \tag{11}$$

Where S is the shear strain rate tensor and Ω is the rotation rate tensor and are defined as:

$$S_{ij} = \frac{1}{2} \left(\frac{\partial U_i}{\partial x_j} + \frac{\partial U_j}{\partial x_i} \right) \tag{12}$$

$$\Omega = \nabla \times \vec{u}$$

Positive Q values indicates regions where the vorticity overcomes shear strain rate. A criterion to identify the presence of a vortical coherent structure is to find out surfaces where Q assumes positive values. Figure 6 and 7 shows the structures observed through the Q criterion around the body.

Zhang et al. (2015) proposed a conceptual model for the flow structure of the high-drag regime around the tridimensional Ahmed body with $\varphi = 25^\circ$. In this model, the authors showed that the flow separates and then reattaches near the leading edge of body's upper part, as seen in Figure 5b. There was also a pair of three-dimensional hairpin vortices, emanating from the recirculation bubble and advecting downstream along the upper surface. Figure 6 shows the presence of the recirculation bubble on the front roof and the presence of a vorticity zone that extends even after the body. The gray surface indicates the positive values for Q variable.



Figure 6. Longitudinal vortices evaluated by Q criterion ($\varphi = 25^\circ$).

According to Möller and Silvestrini (2004), coherent structures can be defined as a large-scale turbulent fluid mass with correlated and phase vorticity in the fluid. Both appear in low Reynolds numbers as a characteristic of the flow symmetry break, but are still observed in high Reynolds values typical of ground vehicles.

As seen by Minguez and Pasquetti (2008) and Zhang et al. (2015), two larges counter-rotating trailing vortices were formed behind the body. In fact, in Figure 7a, the instantaneous streamlines suggest two recirculation bubbles, that show little differences in size. Such difference becomes even more evident as the slant angle is increased.

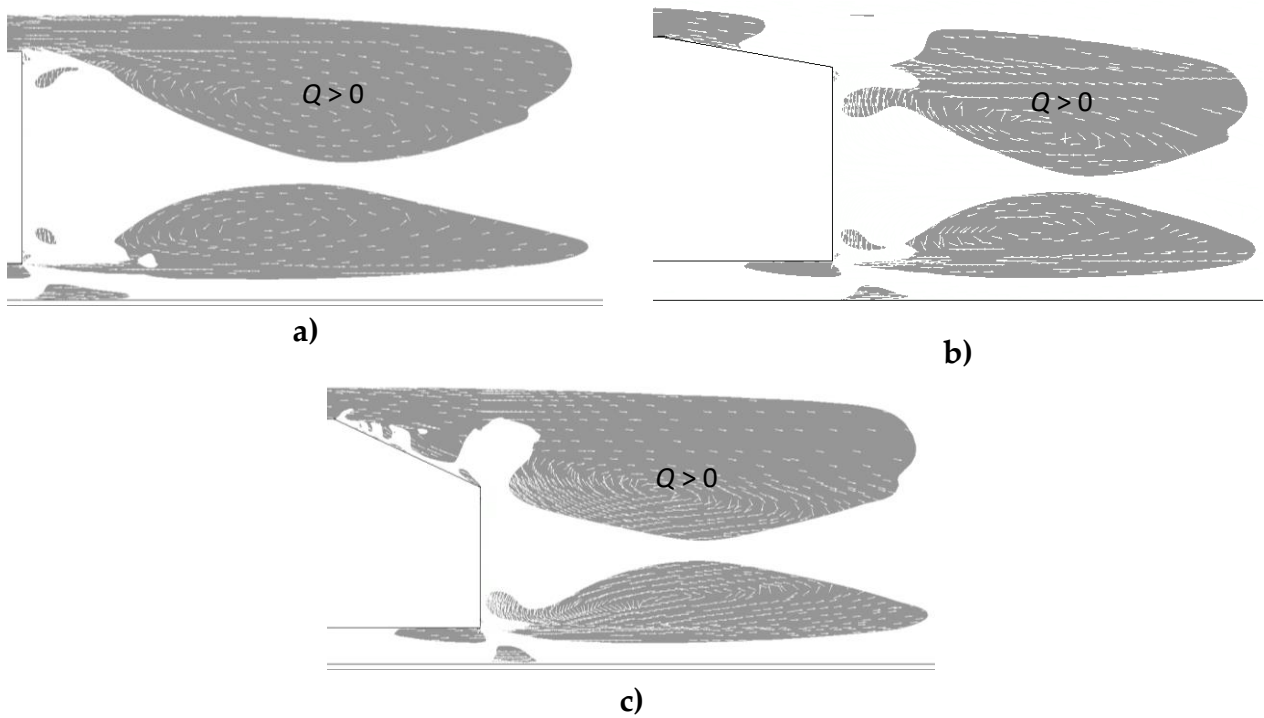


Figure 7. Coherent structures evaluated by Q criterion and velocity vectors: a) 0° , b) 10° and c) 25° .

In addition, C_f indicated that in the body with slant of 10° the flow detaches only after the slanted region ends. The streamlines in Figure 7b show this behavior and allow the reader to visualize the difference when compared with the body of 25° in Figure 7c, where the flow detaches as soon as the slant begins.

3.3. Drag Coefficients

In the present work, the Reynolds number is lower than that used in the Ahmed et al. (1984) in their experiments. Thus, higher values for the drag coefficient are expected than those obtained by Ahmed et al. (1984). This behavior was observed by Thacker et al. (2012), Dobrev and Massouh (2014) and Bello-Millán et al. (2016). Figure 8a shows the values of drag coefficients obtained in the simulations. The lowest drag coefficient was found in the body of $\varphi = 10^\circ$ and the higher one in the body with whose rear slat angle is $\varphi = 0^\circ$. The drag decreases as the φ increases from 0° to 10° degrees. The C_d almost recovers its value again reaching about 0.48 (at $\varphi = 25^\circ$).

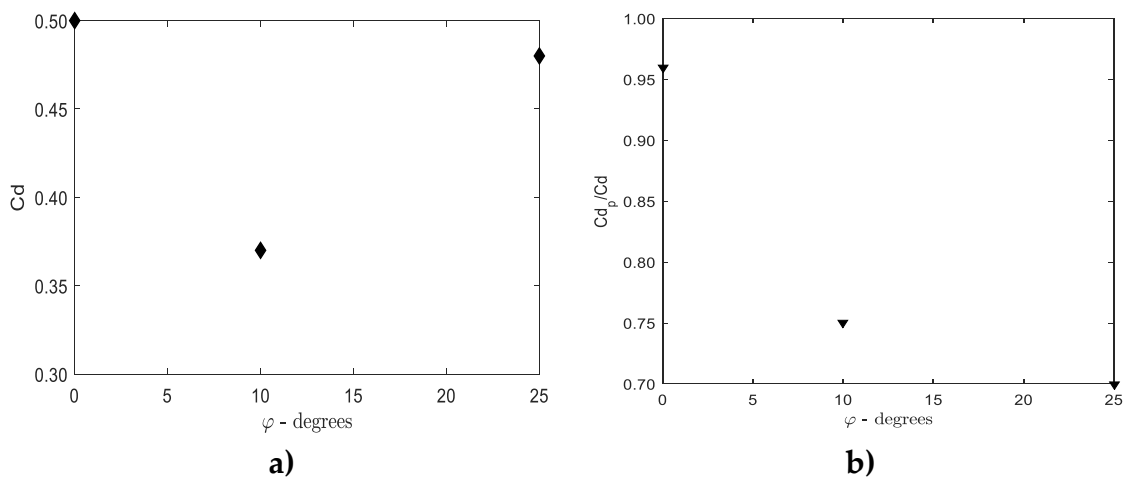


Figure 8. a) Drag coefficients and b) Pressure drag relation on Ahmed body for $Re = 94000$.

As mentioned, our test case (body with $\varphi = 25^\circ$) reached a really good agreement with the Equation 1, proposed by Bello-Millán et al. (2016) and with the work of Rafee and Moghimi (2018) for the same Reynolds number. According to Equation 1 the C_d should be found at 0.44. In our computation we found $C_d = 0.48$.

Ahmed et al. (1984) also noticed the behavior of C_d as function of the rear slant observed in this research. The authors found that a slant angle of 0° leads to a high drag coefficient, but there is also a range of angles that induce more drag on the body. The drag coefficient decreases, as the angle is increased from 0° up to 10° , and increases again until it reaches its critical angle, where the coefficient is maximum. After the critical angles, the drag coefficient falls again. For $Re_L = 4.29 \times 10^6$, this critical angle was 30° .

Figure 8b shows the relationship between the drag portion due to pressure drag C_{d_p} and the total drag coefficient of the body C_d . The C_{d_p}/C_d ratio was found to be from 0.95 up to 0.70, indication that the slant angle leads to a body less blunt. See that the null rear slant yields a C_{d_p}/C_d ratio more than 95%, very typical value found in circular cylinders and blunt bodies.

It is noteworthy the fact that the drag pressure decreases as the slant angle increases, which is very well justified since the area behind the body decreases as the slant rear angle becomes sharper.

5. Conclusions

In the present work, the turbulent flow around Ahmed body was evaluated through time-dependent simulations of the two-dimensional body. The simulations were made for Reynolds number 94 000 for three different rear slant angles, ranging from 0° up to 25° . The turbulence model adopted was the k- ω SST.

It was seen that the pressure coefficient distribution was disturbed by the slant presence. In fact, the stagnation point has been displaced towards the upper surface of the body as slant was increased. In all three cases, C_p tends to present negative values along the body's length as seen by Bruneau et al. (2014).

The skin friction coefficient was equally affected by the slant presence. For $\varphi = 0^\circ$, there was an evidence of flow detachment at the upper side of the body, nearby $x/L = 0.1$. However, there was no evidence of detachment at the end of the body. On the other hand, for the following simulated cases, the skin friction showed points of detachment and reattachment along the body, at almost same position $x/L = 0.49$. Near the body rear, where it is expected that the flow detaches, C_f decreased. For $\varphi = 25^\circ$, C_f indicated a detachment starting at the slanted surface. The recirculation bubble over the body was displaced in comparison with the case $\varphi = 0^\circ$ and the other two cases.

The drag coefficient for $\varphi = 25^\circ$ was found accordingly the equation proposed by Bello-Millán et al. (2016) and agrees with the studies of Rafee and Moghimi (2018). The furthered findings, $\varphi = 0^\circ$ and 10° , showed the C_p recover for $\varphi > 10^\circ$. Further, as the rear slant angle increases the body was seen less blunt and the C_{d_p}/C_d – ratio was seen decreasing as the rear angle increases.

Acknowledgments: Jalusa Ferrari thanks to FAPDF for supporting her with financial resources through the projects n° 193.001.158/2015, 193.001356/2016. Fábio Kayser would like to thank the Coordenação de Aperfeiçoamento de Pessoal de Nível Superior - Brasil (CAPES) - Finance Code 001, for supporting him during this research with a fellowship. Prof. Jhon Goulart is also thankful to CNPq and FAPDF for supporting him with financial resources through the projects n° 193.001.158/2015, 193.001356/2016 and 408869/2016-0.

References

1. Ortega, J. M.; Salari, K. "Aerodynamic drag reduction apparatus for wheeled vehicles in ground effect". [S.l.]: Google Patents, US Patent 6,974,178, 2005.
2. Tunay, T.; Sahin, B.; Ozbolat, V. "Effects of rear slant angles on the flow characteristics of Ahmed body". *Experimental Thermal and Fluid Science*, Elsevier 2014, v. 57, p. 165–176.
3. Wang, Y, et al. "Reduction in the aerodynamic drag around a generic vehicle by using a non-smooth surface." *Proceedings of the Institution of Mechanical Engineers, Part D: Journal of Automobile Engineering* 231.1 (2017): 130-144.
4. Hucho, W. H. "Aerodynamics of road vehicles: from fluid mechanics to vehicle engineering". [S.l.]: Elsevier, 2013.
5. Daugherty, R. L. "Fluid mechanics with engineering applications". [S.l.]: Tata McGraw-Hill Education, 1989.
6. Ahmed, S. R.; Ramm, G.; Faltin, G. "Some salient features of the time-averaged ground vehicle wake". *SAE Transactions* 1984, JSTOR, p. 473–503.
7. Li, Ruiying, et al. "Drag reduction of a car model by linear genetic programming control." *Experiments in Fluids* 58.8 (2017): 103.

8. Essel, Ebenezer, Subhadip Das, and Ram Balachandar. "Effects of Rear Angle on the Turbulent Wake Flow between Two in-Line Ahmed Bodies." *Atmosphere* 11.4 (2020): 328.
9. Siddiqui, N. A., and M. A. Chaab. "A Simple Passive Device for the Drag Reduction of an Ahmed Body.", 2020.
10. Choi, Haecheon, Woo-Pyung Jeon, and Jinsung Kim. "Control of flow over a bluff body." *Annu. Rev. Fluid Mech.* 40 (2008): 113-139.
11. Chovet, Camila, et al. "Sliding mode control applied to a square-back Ahmed body." *European Journal of Mechanics-B/Fluids* 81 (2020): 151-164.
12. Menter, F. R. "Two-equation eddy-viscosity turbulence models for engineering applications". *AIAA journal* 1994, v. 32, n. 8, p. 1598–1605.
13. Korkischko, I.; Meneghini, J. R. *Investigação experimental e simulação numérica do escoamento ao redor de um modelo automobilístico: corpo de Ahmed. Trabalho de conclusão de curso em Engenharia Mecânica apresentado à Escola Politécnica da Universidade de São Paulo, 2006.*
14. Rafee, P. Moghimiand R. "Numerical and Experimental Investigations on Aerodynamic Behavior of the Ahmed Body Model with Different Diffuser Angles." *Journal of Applied Fluid Mechanics* 2018, 11.4: 1101-1113.
15. Bello-Millán, F. et al. "Experimental study on Ahmed's body drag coefficient for different yaw angles". *Journal of Wind Engineering and Industrial Aerodynamics*, Elsevier 2016, v. 157, p. 140–144.
16. Deschamps, C. J. "Modelos Algébricos e Diferenciais–Turbulência." *III ESCOLA DE PRIMAVERA EM TRANSIÇÃO E TURBULÊNCIA 2002*: 100-155.
17. Severino, H. A., De Melo, T., & Goulart, J. N. Hot wire anemometry and numerical simulation applied to the investigation of the turbulence in a gap flow. In *Proceedings of the European Congress on Computational Methods in Applied Sciences and Engineering 2018*. Glasgow, UK.
18. Bruneau, C. H., Creusé, E., Gilliéron, P., & Mortazavi, I. "Effect of the vortex dynamics on the drag coefficient of a square back Ahmed body": *European Journal of Mechanics-B/Fluids* 2014, Vol 45, 1-11.
19. Shadmani, S., et al. "Experimental investigation of flow control over an Ahmed body using DBD plasma actuator." *Journal of Applied Fluid Mechanics* 2018, 11.5: 1267-1276
20. Hunt, J. C. R., Wray, A. A. and Moin, P. "Eddies, Streams, and Convergence Zones in Turbulent flows," *Center for Turbulence Research Report CTR-S88 1988*, Stanford Univ., pp. 193–207.
21. Goulart, Jhon, Jan G. Wissink, and Luiz C. Wrobel. "Numerical simulation of turbulent flow in a channel containing a small slot." *International Journal of Heat and Fluid Flow* 61 (2016): 343-354.
22. Candela, Diana Sandoval, et al. "Numerical simulation of turbulent flow in an eccentric channel." *European Journal of Mechanics-B/Fluids* (2020).
23. Ferrari, J., Goulart, J., & Souza, S. "Numerical Prediction of Pressure Drop and Laminar Instabilities in Fully-Developed Flow in a Closed Compound Channel". *ECCOMAS 2016*.
24. Zhang, B. F., Y. Zhou, and S. To. "Unsteady flow structures around a high-drag Ahmed body." *Journal of Fluid Mechanics* 2015, 777: 291-326.
25. Möller, S.; Silvestrini, J. "Turbulência: fundamentos". *Coleção Cadernos de Turbulência*. ABCM. Rio de Janeiro, v. 4, p. 1–32, 2004.
26. Minguez, M., R. Pasquetti, and E. Serre. "High-order large-eddy simulation of flow over the "Ahmed body" car model." *Physics of fluids* 2008, 20.9: 095101.
27. Thacker, A. et al. "Effects of suppressing the 3d separation on the rear slant on the flow structures around an Ahmed body". *Journal of Wind Engineering and Industrial Aerodynamics*, 2012, Elsevier, v. 107, p. 237–243.
28. Dobrev, I.; Massouh, F. "Investigation of relationship between drag and lift coefficients for a generic car model". *BULTRANS Proceedings* 2014.